Multipitched plasmonic nanoparticle grating for broadband light enhancement in white light-emitting organic diodes

Manuel Auer-Berger[1] · Veronika Tretnak[2] · Christian Sommer[1] · Franz-Peter Wenzl[1] · Joachim R. Krenn[2] ·
Emil J. W. List-Kratochvil[3,4]

Abstract

We apply regular arrays of plasmonic nanodisks to enhance light emission from an organic white light-emitting diode (WOLED). To achieve broadband enhancement, we apply, first, aluminum as a nanodisk material with moderate loss throughout the whole visible spectral range. Second, broadband light coupling is mediated by surface lattice resonances from a multipitch array built from two superimposed gratings with different grating constants formed by elliptic and circular nanodisks. To demonstrate the viability of this concept, the grating structure was embedded in the hole transport layer of a solution-processed phosphorescent WOLED exhibiting a current efficiency of 2.1 cd/A at 1000 cd/m^2. The surface lattice resonances in the grating raise the current efficiency of the device by 23% to 2.6 cd/A at 1000 cd/m^2, while the device emission changes from a neutral white to a warm white appearance with CIE1931 (x,y) coordinates of (0.361, 0.352) and (0.404, 0.351), respectively. The WOLED was characterized in detail optically by extinction and angle-resolved photoluminescence and as well by electroluminescence measurements for its opto-electronic characteristics. The experimental results agree well with finite-difference time domain simulations that aim at a better understanding of the underlying physical mechanisms. In summary, our work presents a novel versatile approach for achieving broadband enhancement of light emission in WOLEDs over a wide spectral range.

1 Introduction

Over the course of the last decades, organic light-emitting diodes (OLEDs) have emerged as a viable technology for display applications on the verge of capturing a majority share of the small display market [1]. With thermally activated delayed fluorescence [2, 3] as well as phosphorescent emitter systems [4, 5] exhibiting high internal quantum efficiencies (IQE) of close to 100%, the foundation for the application of OLEDs in the lighting segment was laid. Here, the prospect of flexible and/or large area luminaries obtainable by low-cost roll-to-roll processes is intriguing. Presently, however, depending on the emission color relatively low external quantum efficiencies (EQE) of only 15–45% [2, 6] low lifetimes prove to be formidable stumbling blocks for OLEDs in the lighting market. With the attainable IQE already being close to unity, it is evident that to significantly improve the EQE one needs to tackle light trapping processes in the device, which are caused [6] by surface plasmon polaritons (SPPs) at the organic-metal interface and guided optical- and substrate modes in the active device stack. Several concepts have been proposed to counter these loss mechanisms and hence to increase the amount of extracted light [7, 8]. The most straightforward solution to drastically reduce light trapping is to align the dipole emission with the direction normal to the OLED

✉ Emil J. W. List-Kratochvil
emil.list-kratochvil@hu-berlin.de

1 JOANNEUM RESEARCH Forschungsgesellschaft mbH, Franz-Pichler Straße 30, 8160 Weiz, Austria

2 Institut für Physik, Karl-Franzens-Universität Graz, Universitätsplatz 5, 8010 Graz, Austria

3 Institut für Physik, Institut für Chemie, IRIS Adlershof, Humboldt-Universität zu Berlin, Zum Großen Windkanal 2, 12489 Berlin, Germany

4 Helmholtz-Zentrum Berlin für Materialien und Energie GmbH, Hahn-Meitner-Platz 1, 14109 Berlin, Germany

plane. Even though this solution would be generally preferable, the mechanism behind obtaining dipole orientation is not clearly understood [1] and successful demonstrations are so far limited to monochromatic OLEDs [6, 9, 10] containing only one emitter. Here, we exclude molecular engineering and concentrate on schemes that rely on the modification of the device stack to extract light more efficiently. Corresponding approaches include Bragg gratings [11], integrated 2D photonic crystals [12], internal scattering layers [13], micro-lens arrays [14], high refractive index glass [15], and specific substrate surface patterning techniques [16], to only name a few.

Another outcoupling scheme relies on regular arrays of plasmonic nanoparticles (NPs). The regular 2D particle arrangement gives rise to diffraction in specific directions, as commonly exploited with light from an external source incident onto a (1D or 2D) grating. For arrays formed by plasmonic NPs, the light fields of grating orders diffracted along the array plane can strongly couple to the localized plasmon resonances (LSPRs) of the NPs. Thereby, hybrid light/plasmon modes form, so-called surface lattice resonances (SLRs) [17, 18] that signify particularly strong light/matter interaction and that can lead to spectral modifications and a strong near field enhancement, as compared to an irregular NP array [19]. When a regular array of plasmonic NPs is embedded in a light-generating layer, the outcoupling of light is facilitated by grating diffraction (by design, preferably in the direction normal to the OLED layers) for a range of wavelengths that is determined by the NP distance, i.e., the particle grating pitch [20]. In addition, upon direct interaction with the light-generating entities, the resonantly enhanced plasmonic near fields can significantly alter their emission properties in terms of excited state lifetime, emission profile and (for intrinsically poor emitters) IQE [21].

The proof-of-principle of NP array modified emission was demonstrated for photoluminescence (PL) from a single emissive layer [22]. It should be noted that earlier work already showed plasmon-mediated outcoupling enhancement from an OLED, however, for a modulated metal surface without LSPRs [23]. In Ref. [24], emission modifications from a single-emitter OLED were reported. A recent approach embedded a plasmonic NP array within an organic light-emitting field effect transistors [25], resulting in substantially enhanced emitted light intensities. Typically, silver or gold NPs are used for their rather low damping, but recently aluminum (Al) was also found to show surprisingly good plasmonic properties in the spectral UV-to-NIR range [26, 27]. Combined with its self-passivating properties and abundant nature, Al is a particularly intriguing candidate as the base material for SLR-supporting plasmonic arrays suitable for enhanced broadband light generation and extraction. While Al NP arrays have indeed been extensively studied to enhance the efficiency of color converting layers

for inorganic light-emitting diodes (LEDs) [22], we have recently shown that Al NP arrays enable to tune the emission color [28] and to enhance the performance of blue-emitting phosphorescent OLEDs by 35% [29]. Extending this concept to be applicable for white-light-emitting OLEDs (WOLEDs) would be a welcome addition for designers of luminaires to enhance device efficiencies, while at the same time benefiting from fine-color adjustments. Obviously, a major hurdle originates from the fact that these SLRs are usually only active for one spectral band (red, green or blue), which makes it difficult to exploit for broadband enhancement across the entire spectral range of a WOLED stretching from blue to red.

To mitigate that issue, we here propose a new approach by designing and implementing a structure addressing multiple spectral bands, consisting of a multipitched array formed by two superimposed particle gratings that are built from differently shaped disk-shaped NPs. One grating comprises elliptic nanodisks (NDs), while the other is built from circular NDs. Compared to, e.g., line-gratings, this provides the benefit of individual spectral tuning of the plasmonic resonances by means of ND shape and grating pitch and thereby to obtain optimal enhancement in the relevant spectral regions. At the same time, ND gratings can be fully embedded into the solution-processed hole transport layer (HTL) of the WOLED, minimizing obstruction of the device performance. Through angle-resolved PL and electroluminescence (EL) spectroscopy, we demonstrate clearly that the SLRs induced by the superimposed gratings truly cover the relevant parts of the luminosity function for a human observer from 480 to 620 nm and indeed enhance the current efficiency of the WOLED. The presented device-related work is supported by detailed measurements using optical spectroscopy and finite-difference time domain (FDTD) simulations.

2 Experimental section/methods

2.1 Materials and WOLED preparation

Copper (I) thiocyanate (CuSCN), diethyl sulfide (<99%) (DES), tetrahydrofuran (<99.9% HPLC) dichloromethane (<99.9% HPLC) and polymethyl methacrylate (PMMA) were purchased from Sigma-Aldrich. Bis(3,5-difluoro-2-(2-pyridyl)phenyl-(2-carboxypyridyl)iridium(III) (FIrpic), Tris[2-phenylpyridinato-C2,N] iridium(III) Ir(ppy)3, Tris(1-phenylisoquinoline)iridium(III) ((Ir(piq)3), Tris(4-carbazoyl-9-ylphenyl)amine (TCTA), 4,4′-Cyclohexylidenebis[N,N-bis(4-methylphenyl) benzenamine] (TAPC) and 1,3,5-Tris(3-pyridyl-3-phenyl)benzene (TmPyPB) were purchased from Luminescence Technology Corp. (LUMTEC) and used as received.

Float glass coated with 100 nm indium tin oxide (ITO) (15 Ω sq^{-1}) was purchased from Kintec Hong Kong. The ITO substrates were treated in ultrasonic baths of 2 vol% Hellmanex III for 20 min at a temperature of 50 °C. The substrates were then carefully rinsed with deionized water after which another 10 min of ultrasonication in acetone and isopropyl alcohol (IPA) followed. The cleaning was completed by a final IPA rinsing and nitrogen dry-blowing step. A 100 nm thick layer of PMMA was spin coated followed by a bake-out at 180 °C for 5 min. The sample was subsequently transferred into a RAITH e-line plus electron beam lithography (EBL) system, and the whole structure consisting of two superimposed rectangular ND gratings was exposed to the resist. After developing the sample, a 20 nm thick layer of aluminum was thermally evaporated, followed by a lift-off step using acetone. Scanning electron microscope (SEM) images were recorded in the EBL system using the in-lens secondary electron detector. The ITO substrates with the superimposed Al gratings were rinsed with acetone and IPA before subjecting them to an ultrasonication treatment for 10 min. The cleaning was completed by a final IPA rinsing and nitrogen dry-blowing step.

CuSCN [30] was dissolved at a concentration of 22 mg ml^{-1} in DES and stirred for 1 h. For spin-coating, the solution was applied to the patterned and cleaned substrates with a syringe complimented by a suitable 0.2 µm polytetrafluoroethylene filter. The spin-coating parameters were set to yield a film thickness of approximately 50 nm. After spin-coating, the substrates were baked at 120 °C for 5 min before transferring them to an argon-filled glovebox. Via atomic force microscopy (AFM), we show that finally the ND array is fully embedded in the solution-processed CuSCN HTL.

The emissive layer (EML) was prepared by adding the host molecules TCTA and TAPC in a 3:1 ratio in a 1:1 mixture of DCM/THF. The concentration of the solution was set to 10 g/L. FIrpic was added to the solution as a blue dopant at a concentration of 15 wt% FIrpic, while 0.1 wt% of the green-emitting Ir(ppy)$_3$ and 0.6 wt% of the red-emitting (Ir(piq)$_3$ were added to the solution. Spin-coating parameters were chosen to yield a 65 nm thick layer. After spin-coating, the substrates were baked at 110 °C under high vacuum for 30 min before they were transferred to an evaporation chamber, where 45 nm of 1,3,5-Tris(3-pyridyl-3-phenyl) benzene (TmPyPb) [25] was deposited at a base pressure of 10^{-6} mbar as electron transport layer (ETL). For WOLED characterization, an active area of 1.5 × 1.5 mm [2] was defined by depositing the cathode with 1-nm-thick Ca as electron injection layer (EIL) and 100-nm-thick Al through a shadow mask.

Current/luminance/voltage (I–L–V) characteristics were recorded in a customized setup. To determine the I–V characteristics, a Keithley 2612A source measurement unit was used. A calibrated photodiode connected to a Keithley 6485 picoamperemeter was employed to record the EL. Angle-resolved EL spectra were acquired using a custom-built goniometer setup with a calibrated LOT-ORIEL Multispec spectrometer equipped with a DB 401-UV charge-coupled device (CCD) camera from Andor.

2.2 AFM topography

AFM topography images were recorded in tapping mode using a Veeco Dimension V. Ellipsometry measurements were carried out on films made by spin-coating the EML and evaporating 45 nm of the ETL on cleaned Si wafers nominally without native oxide (however, the modeling had to include a thin silicon oxide layer with 2 nm thickness). The optical properties and the thickness of the films were derived by means of variable-angle spectroscopic ellipsometry (VASE, J. A. Woollam Co., Inc). Spectra were acquired for a spectral range of 300–1300 nm at angles of incidence of 65°, 70° and 75° with respect to the substrate normal. Modeling of the acquired VASE data was performed using the WVASE software package (J.A. Woollam Co., Inc.). The modeling was based on coupled Lorentzian oscillators and assumed the presence of inhomogeneous thin films exhibiting isotropic behavior.

2.3 Optical characterization

Extinction and fluorescence microscopy measurements of test samples (area < 1 mm^2) were done with a 20× objective and an effectively used full sampling angle of 2.2° as well as with a 5× objective with a numerical aperture of 0.075. Extinction is defined as $1 - R/R_0$ where R is the reflectance of a patterned area and R_0 is the reflectance of a non-patterned area on the same substrate. For PL spectroscopy, a halogen lamp together with an excitation bandpass filter with a center wavelength of 360 nm and a 10 nm bandwidth was used.

Angle-resolved measurements over large areas (2 × 2 mm^2) were carried out using an Instrument Systems Gon360 goniometer setup connected to a CAS 140CT array spectrograph. The goniometer setup had an angular resolution of 0.01° with an accuracy of ±0.3° for the illumination as well as the detection angle. To record the full half-space above the device, the illumination angle of the light from a stabilized halogen source was set to 15°. Angle-resolved PL measurements were carried out with the same goniometer using an UV light source with a wavelength of 365 nm.

2.4 FDTD simulations

FDTD simulations were carried out using FDTD Solutions from Lumerical. For the WOLED geometry, an ultra-fine mesh size of 1 nm was used. The simulation area was defined

by periodic boundary conditions for the lateral dimensions and a perfectly matching layer (PML) in the outcoupling direction as well as a perfect electrical conductor (PEC) in a distance of 30 nm from the ETL/cathode interface. The symmetry of the rectangular array pattern allowed for a reduction in simulation volume. The respective thicknesses of the individual layers of the WOLED stack (as input values for the simulations) were known with an error of ± 2 nm, as after full PL/EL characterization the devices were disassembled in a layer-by-layer fashion for measuring layer thicknesses by AFM. In the simulations, the electric field intensity inside the EML was recorded using a volume monitor, while transmission or reflectance spectra were recorded by a field monitor placed 300 nm from the layer structure. As the light source, a plane wave illumination was chosen.

Dipole simulations were performed considering an area of 15×15 μm². To model the incoherent nature of dipole relaxation inside a WOLED, the simulation was repeated for different dipole polarizations and positions. Enhancements were calculated by normalizing to the simulation results for a WOLED without a grating. To carry out the simulation, the mesh size had to be coarse along the lateral directions with a 20 nm spacing, while the z-direction was discretized with a 10 nm spacing.

3 Results and discussion

3.1 Optical characterization of multipitched Al ND grating

Figure 1 shows a sketch of the WOLED stack as used in this study and a SEM image of a representative section of the Al ND array fabricated by electron beam lithography (see Sect. 2). We note that this is a flexible but rather slow method; however, the involved structure dimensions could as well be achieved with scalable techniques as nanoimprinting. The requirements for the grating design were to include three different ND LSPRs for effective coupling to the molecules, and to provide distinct SLRs for every emission wavelength. This was achieved by using two different ND shapes. First, a circular ND (diameter 80 nm, height 20 nm) with a plasmon resonance in the blue wavelength range and, second, an elliptically shaped ND with different resonances along the long (140 nm) and short (70 nm) axis, again with a height of 20 nm. The grating pitches were fixed at 310 nm in the x-direction for the elliptic NDs and at 280 nm for the circular NDs, while the grating constant in y-direction was uniformly set to 340 nm.

In Fig. 2, we show the extinction spectra of the broadband multipitched Al ND array depicted in Fig. 1b. The spectral extinction was probed with unpolarized incident light as well as with light polarized along both main axes of the elliptic NDs, i.e., with x- and y-polarization. The spectral positions of the SLRs in this sample were adjusted to the
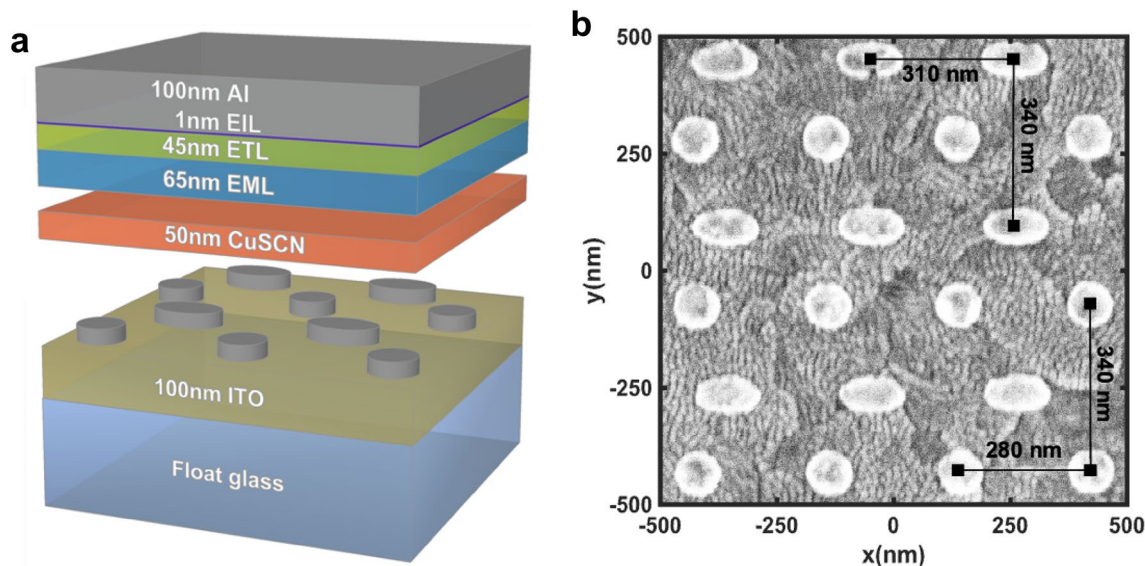

Fig. 1 **a** Sketch of WOLED device stack with a multipitched Al ND grating and the device layers (Al ND array processed on ITO, a 50-nm-thick CuSCN HTL, a 65-nm-thick EML, a 45-nm-thick ETL and a cathode comprising 1 nm of EIL and 100 nm of Al; for fur-ther details, see text in the device section). **b** Top-view SEM image of the superimposed Al ND array with the grating constants along the x- and y-directions
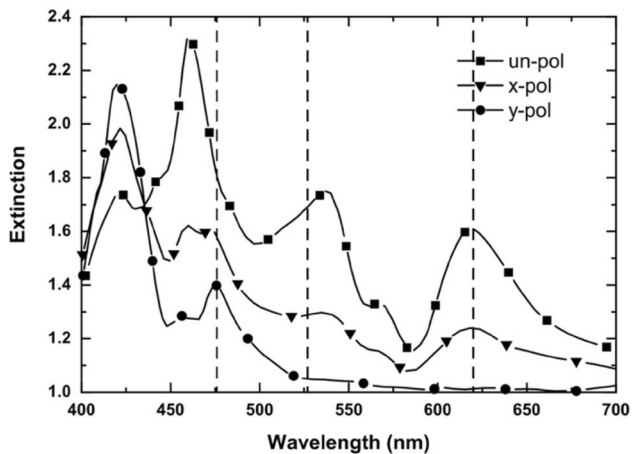
Fig. 2 Measured extinction spectra of a superimposed ND broadband grating with dimensions as shown in Fig. 1b for unpolarized, *x*-polarized and *y*-polarized light. The vertical black lines indicate the wavelength of the emission maxima of FIrpic (blue emitter), Ir(ppy)$_3$ (green emitter) and Ir(piq)$_3$ (red emitter)

waveguide modes of the WOLED with an expected mode index of $n = 1.7$. Considering the expression for the first grating order $\sin\theta = \pm\lambda/nd$ (θ diffraction angle, n effective refractive index of the medium embedding the grating, d grating pitch), the condition relating grazing orders ($\theta = 90°$) and light propagating perpendicular to the grating plane simply reads $\lambda = nd$. Accordingly, the chosen grating pitches lead to SLRs around wavelengths of 476, 527 and 620 nm, corresponding to the three emitters. Most importantly, in the spectra we observe broadband extinction over the whole visible spectral range with various specific features at the designed energies that in turn are expected to couple light out of the WOLED. Concerning the detailed interpretation of these features we have, however, to emphasize two points. First, while the grating geometry was designed for operation in the WOLED, we first analyzed its optical response (as shown in Fig. 2) following fabrication on bare ITO, i.e., before the addition of the further WOLED layers.

The asymmetric environment can lead to spectral shifts of the SLR and LSPR features that are difficult to consider in simple terms. Second, spectrally close SLR and LSPR features can hybridize, i.e., interact in terms of energetic repulsion, leading to peak anticrossing and complicating their spectral signatures [31, 32]. Nevertheless, we briefly discuss the main features in the spectra in Fig. 2, beginning with the *x*-polarized case. This excitation condition leads to LSPRs that basically resemble dipoles oriented in *x*-direction. Their main emission is thus in *y*-direction, making the grating pitches in *y* (together with the ND dimensions in *x*) the relevant parameters. The peak around 420 nm that is far from the expected SLR positions can be assigned to the circular ND LSPR, while the long axis elliptical LSPR

is evidenced by the prominent peak at 620 nm. The features around 550 nm are due to the long wavelength SLR, while the strong peak around 460 nm is most likely due to a higher order SLR introducing polarization crosstalk, a fact that deserves further investigation. For *y*-polarized light, we find an intense peak around 420 nm due to both LSPRs of the circular ND and the short axis elliptical ND. Around 450 nm, a SLR signature dominates the spectrum. For unpolarized illumination, we find the expected superposition of the two spectra taken with polarized light, further illustrating the broadband character of the grating.

3.2 Implementation of the multipitched Al ND grating in the WOLED stack

As a first step toward assessing the performance of the fabricated embedded Al ND array in the WOLED stack, it needs to be verified that the array does not introduce additional leakage current through the formation of shunts, thus hampering current efficiency. Generally, a ND height of 20 nm must be considered a relevant distortion for the overall 160 nm thickness of the organic layers of the WOLED stack. Previously, we found that Al ND arrays can indeed be embedded in the HTL, resulting in very smooth HTL layers [28, 29]. Yet, in the present case the Al ND array is more complex and noticeably denser, covering almost 18% of the surface area, as compared to 12% in the former studies.

AFM topography images as depicted in Fig. 3a–d were acquired over an area of 1.5×1.5 μm^2. The bare Al ND array features a root mean square (RMS) surface roughness of 11.4 nm, which is, however, strongly reduced to 4.2 nm after the deposition of the CuSCN layer (Fig. 3a and b, respectively). Indeed, the RMS roughness is found to be practically identical to the surface roughness of CuSCN formed on bare ITO, as depicted in Fig. 3c. For the entire WOLED stack (measured on the ETL), we find a low surface roughness of only 0.6 nm and thus efficient planarization, which confirms that our approach for embedding the Al ND array works as anticipated (Fig. 3d).

To evaluate the effectiveness of the Al ND array in a WOLED, we chose a state-of-the-art solution-processed triple layer device stack as described in Ref. [33]. The used semiconducting materials, the according energy levels (as obtained from literature) as well as the triplet energy levels of the individual device layers are depicted in Fig. 4. An efficient injection of holes from ITO into the EML is provided by CuSCN. The EML consists of a 3:1 blend of TCTA and TAPC to which TAPC provides a more ambipolar charge carrier transport necessary for obtaining efficient WOLEDs. To achieve an emission appearing whitish, a blend consisting of the three phosphors FIrpic, Ir(ppy)$_3$ and Ir(piq)$_3$ is used. Blocking of hole injection as well as efficient electron injection is provided by TmPyPb, which has a low-lying

Fig. 3 AFM topography images of **a** an Al ND array on ITO, **b** an Al ND array embedded in CuSCN (RMS roughness 4.2 nm), **c** CuSCN coated on top of bare ITO (RMS roughness 4.2 nm) and **d** a full WOLED device stack, with the ETL as the uppermost layer (RMS roughness 0.6 nm)
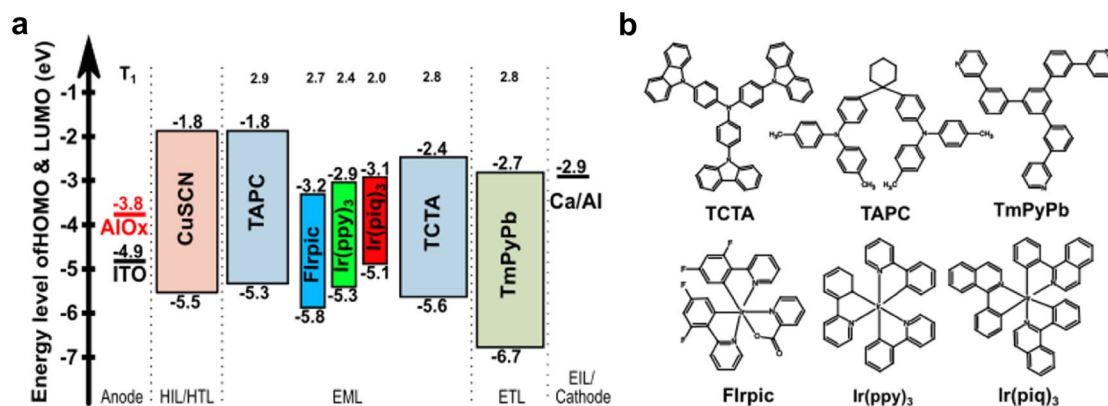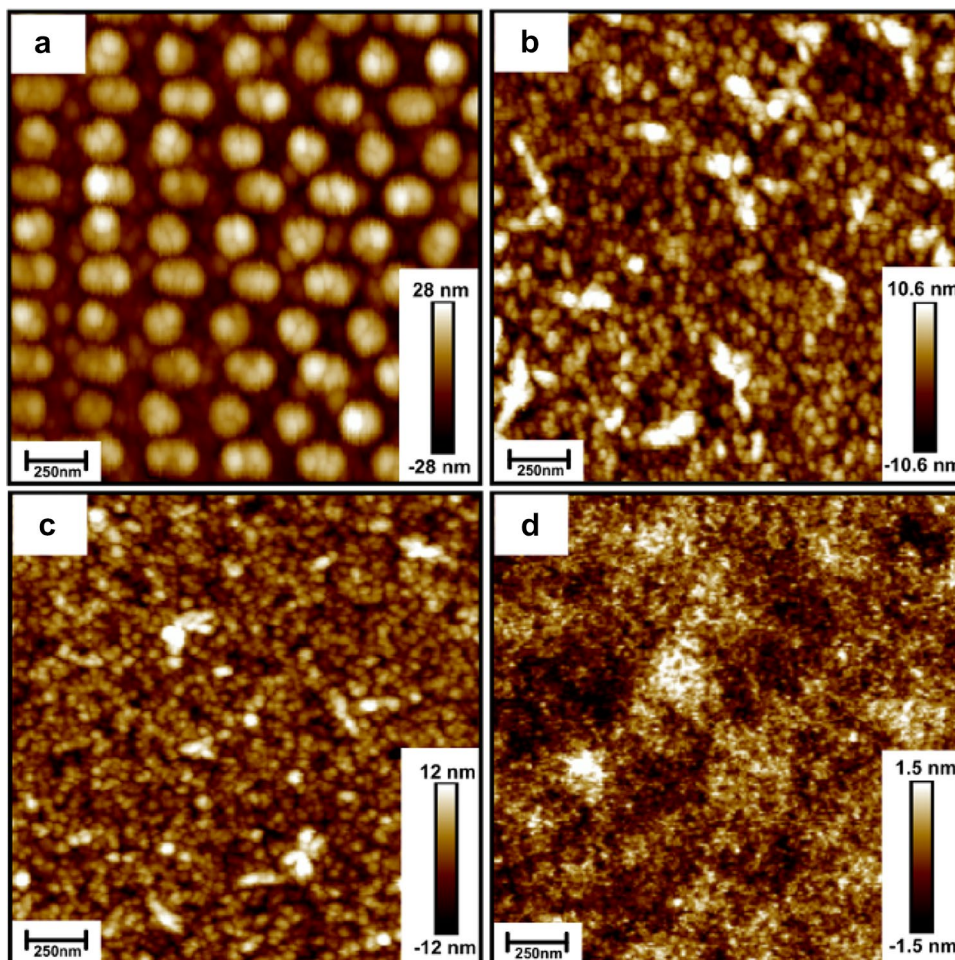

Fig. 4 **a** Energy levels (HOMO and LUMO) of the individual layers in the WOLED stack, work functions of electrodes and triplet energies T1 of the used organic semiconductors as given in the literature (ITO and AlOx [35], CuSCN [36], EML [33], ETL [33], and cathode [35]) **b** chemical structure of the organic semiconductors used in the WOLED stack.

highest occupied molecular orbital (HOMO) and a lowest unoccupied molecular orbital (LUMO) level well aligned with the work function of the cathode consisting of Ca covered with Al for protection. The triplet energies of the used transport layers are high enough to achieve sufficient confinement of triplet excitons in the EML.

The results of the electro-optical WOLED characterization are summarized in Fig. 5, while the key performance
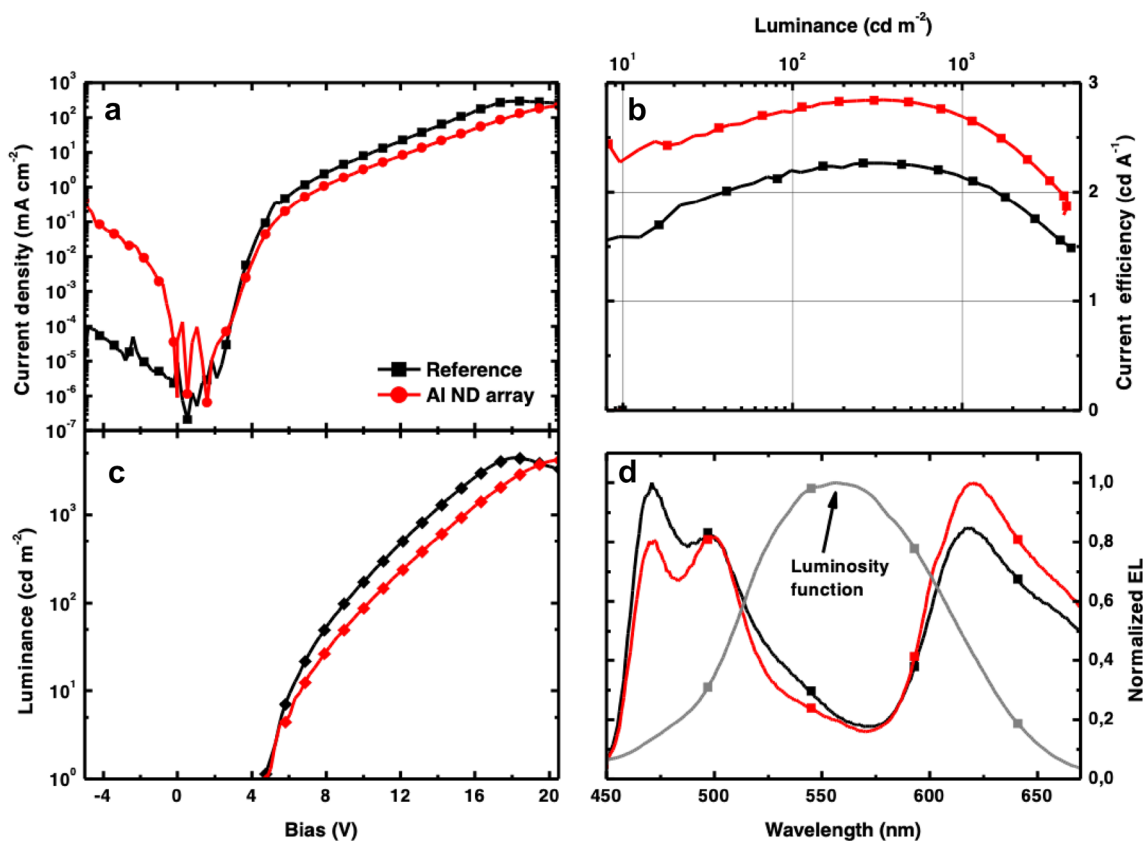
Fig. 5 Device characteristics for a WOLED with embedded Al ND array (red symbols) and a reference device (black symbols). **a** Current density- and **b** luminance versus applied bias voltage, **c** current efficiency versus luminance and **d** normalized EL emission spectra. The gray line depicts the luminosity function of the human eye. For clarity, only a reduced number of symbols is displayed, the red and black lines are guides to the eye

device parameters are listed in Table 1. Starting the discussion with the current density characteristics (Fig. 5a), a clear drop in current density compared to the unstructured reference device is observed at similar applied bias voltages. At the emission onset (4.7 V), the current density is only 45% of the reference device. Increasing the bias toward 16.8 V, the difference reduces to 31% at a bias of 16.8 V and it vanishes for a bias larger than 20 V. This severe difference is attributed to the 18% coverage of ITO with the Al NDs, which reduces the device current due to significantly obstructed hole injection into the device because of the formation of. ca. 3-nm-thick native aluminum oxide (Al_2O_3) on the ND surface [34]. Given current experimental limitations in device fabrication, which include an unavoidable transfer of the sample in air, we unfortunately cannot remove the oxide or avoid the oxide formation. Remarkably,

Table 1 Key performance device parameters

Device Type	Device Onset[a]	Maximum luminance	Current efficiency		Efficiency enhancement	CIE1931[b]
	(V)	(cd m^{-2})	(cdA^{-1})		(%)	(x,y)
			10^2 cd m^{-2}	10^3 cd m^{-2}	10^3 cd m^{-2}	
Reference WOLED	4.7	4420 (18.2 V)	2.2	2.1	-	(0.361,0.352)
Al ND array WOLED	4.7	4107 (20.3 V)	2.7	2.6	+ 22.8	(0.404,0.351)

[a]At 1 cd m^{-2}

[b]At a current density of 5 mA cm^{-2}

in an earlier report we found almost no deviation in the carrier injection behavior at a total coverage of 12.6% [29], while here at 18% coverage less than half the current density is observable. While at first glance this might be considered unsatisfactory, in the present study the focus was on investigating the superimposed Al ND array and we are confident that optimization of the device fabrication process using an additional reactive ion etching process and interlayer deposition processes within an inert cluster tool to avoid the formation of an Al_2O_3 interlayer in a next step will eliminate the observed injection barriers. Moreover, in reverse bias direction we observe a drastic increase in the leakage current by almost three orders of magnitude as compared to the device without the Al ND array. This is attributed to the additional corrugation introduced into the device stack due to the Al ND array and the fact that the utilized CuSCN HTL can help to only smoothen the corrugation by a limited amount.

The luminance-bias voltage characteristics of the devices without and with Al ND array are shown in Fig. 5c. The device without the Al ND array reaches a maximum luminance of 4420 cd m^{-2} at 18.2 V, while the device with the Al ND array reaches only 4107 cd m^{-2} at 20.3 V. The reduced overall luminance is a clear consequence of a deteriorated hole injection. Even though the overall luminance is reduced in devices with the Al ND array, the corresponding current efficiency (Fig. 5b) increases from 2.1 cd/A (for the device without the Al ND array) to 2.6 cd/A (22.8%), as perceived at 1000 cd m^{-2}. As already mentioned, the introduction of the Al ND array leads to a shift of the most dominant emission band (from the blue emission band with a maximum of 471 nm to the red emission band with a maximum at 621 nm (Fig. 5d) in the spectral power distribution. In accordance, this causes a shift of the CIE1931 (x,y) coordinates from (0.361, 0.352) to (0.404, 0.351) and a shift of the correlated

color temperature from 4434 to 3153 K, which results in a change from a neutral white to a warm white appearance of the device emission.

Still, changes of the EL spectra of the reference and grating device and their respective overlap with the luminosity function may also affect the values of photometric units. However, normalizing both EL spectra to a radiant flux of 1 W shows that this would correspond with a luminous flux of 250.8 lm in case of the reference device and 245.1 lm in case of the device with the grating structure. This slightly lower value of the luminous flux in case of the device with the grating structure is due to the lower sensitivity of the human eye in the red wavelength range, which is enhanced for this device. Therefore, one can conclude that this gain in current efficiency originates from enhanced generation and outcoupling of light. The somewhat lower value for the luminous flux in case of the grating device with the grating structure shows, that this enhancement of light generation and outcoupling is even slightly larger than 22.8% as it is expressed on the base of the above-mentioned enhancement of the overall current efficiency.

3.3 Optical characterization and simulation of the grating WOLED

We now turn to the optical extinction measurement and FDTD simulation of the grating embedded in the WOLED stack. The unpolarized extinction spectrum of the WOLED-embedded Al ND array is depicted in Fig. 6a (black). It is characterized by several emission bands that correspond closely to those found for the superimposed ND grating on ITO (Fig. 2), however, with some spectral shifts, as expected. The experimental data are also rather well matched by the FDTD simulated spectrum (Fig. 6a, blue). In addition,
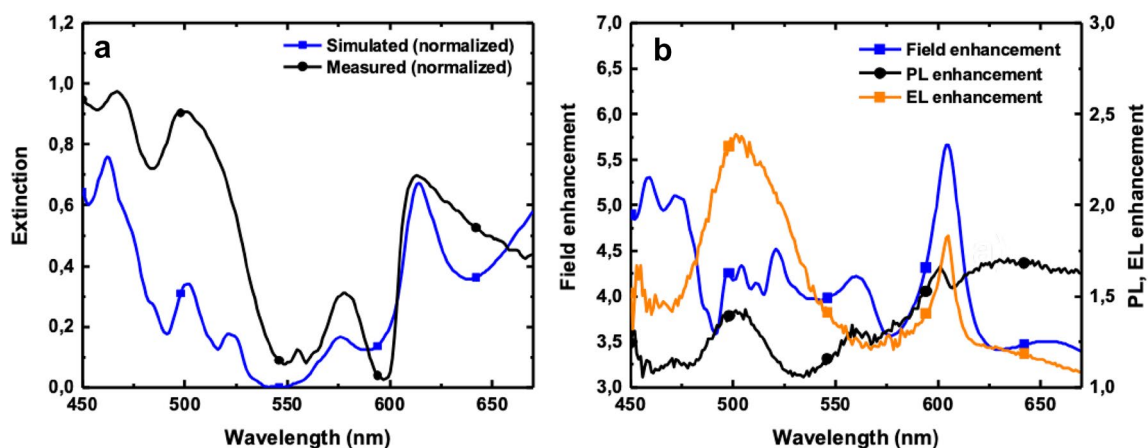

Fig. 6 Spectra of an Al ND arrays embedded in the WOLED stack. **a** Measured (black) and FDTD simulated (blue) extinction spectra, **b** simulated PL (black) and EL (orange) enhancement and induced spectral field enhancement (blue), obtained by integrating over the volume occupied by the emitters. For clarity, only a reduced number of symbols is displayed, the lines are guides to the eye

simulations with polarized excitation (not shown) support the former assignment of the observed extinction peaks to the circular and elliptic ND sub-gratings. The assignments are further supported by FDTD simulation maps of the electric field intensity ($|E|^2$) maps as depicted in the Supporting Information (Figures S1–S4).

The spectral PL enhancement is plotted in Fig. 6b (black), where the enhancement is defined as the ratio of PL from an unstructured WOLED area and PL from the WOLED area including the multipitched ND grating. We find a broad enhancement peak with a maximum enhancement value of 2.5 which can be readily assigned to the ND SLRs generated for y-polarization. Another 1.8-fold enhancement is found at 605 nm, presumably from the SLR due to *x*-polarization. The orange spectrum in Fig. 6b shows the EL enhancement that strongly resembles the basic features of the PL curve, however, with differently weighted absolute values. The blue line in Fig. 6b shows the overall field enhancement, which well explains the 1.8-fold enhancement for the EL emission at 605 nm. This interpretation is again further corroborated by FDTD simulations in the Supporting Information (Figures S1–S4).

In line with our previous findings [28, 29], the observed discrepancy between EL and PL enhancement can be attributed to the preferential excitation of higher order modes as well as to the fact that the whole EML is active in PL, whereas only a relatively small recombination zone contributes to the generation of light under EL in the WOLED. Still worth discussing is the broad enhancement in the low energy part of the spectrum below 600 nm. For this, it is required

to keep in mind that in a WOLED host/guest system with three different molecular emitters, the generation of white light has to rely on the fact that at some point the red emitter, which has the lowest optical bandgap in the system, will saturate because of the high lifetime of phosphorescent emitters. Even though the near field enhancement provided by the LSPR is usually not as high within the EML as the one provided by the SLR, the chosen thickness is low enough to still generate a significant enhancement within the EML. This enhancement could lead to a decrease in the excited state lifetime and thus, a shift of the saturation point toward a higher voltage.

3.4 Angular dependence of emission

So far, we have shown that the efficiency of a WOLED can be effectively enhanced by a multipitched ND grating. To analyze the coupling between guided light modes in the optical stack and the ND grating we turn to angle-resolved PL and EL measurements. For the sake of clarity, the study was done separately on elliptic and circular Al ND gratings. The luminescence enhancement is plotted as the signal level measured on a WOLED including the respective ND grating, normalized to the signal from a WOLED area without grating. The measurements together with the corresponding calculated dispersion relations for x- and y-polarizations are depicted in Fig. 7. The SLR dispersion was calculated through simple grating scattering [22]. We calculated the angle-dependent light emission for *x*- and *y*-polarization upon the interaction of the gratings with the fundamental
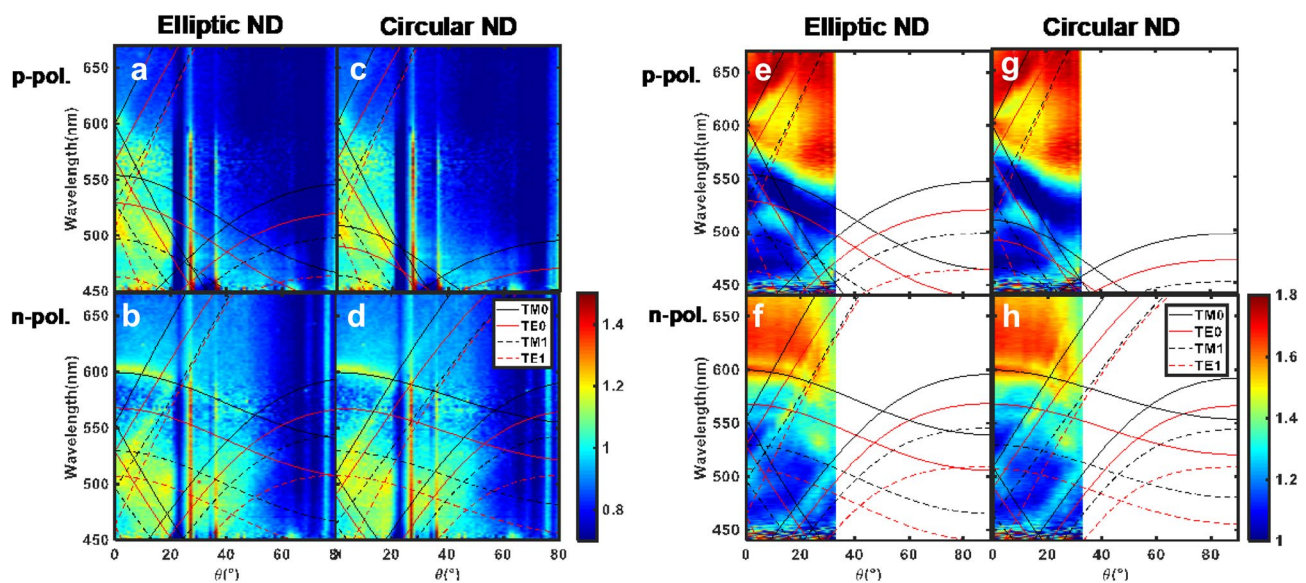

Fig. 7 Measured emission intensity of angle-resolved **a–d** PL spectra and **e–h** EL spectra of a WOLED including elliptic or circular Al ND gratings (color). Separate measurements for elliptic and circular ND gratings are shown for both, *x*- and *y*-polarization, as indicated in the figure. The calculated SLR dispersions are plotted for the waveguide modes listed in the figure legends by the black and red lines

waveguide modes in the WOLED stack, i.e., TM_0, TE_0, TM_1 and TE_1, as identified by the mode solving option of the FDTD Solutions package and depicted in Fig. 7.

Generally, for the angle-resolved PL enhancement (Fig. 7a–d) we achieve a good match between the observed enhancement and the calculated SLR dispersion. For *y*-polarization, we find an enhancement for propagation along the *x*-direction of all considered modes. However, the largest gains clearly stem from slowly dispersive modes in *y*-direction coupling to the TM_0 as well as the TE_1 modes. For normal incidence, these enhancements are spectrally located around 600 (TM_0) and 500 nm (TE_1) (Fig. 7b, d). Exemplary simulated maps of the wavelength dependent modal energy density within the optical WOLED stack are plotted in the Supporting Information (Figure S5).

The angular resolved EL enhancement shows the already discussed pronounced increase in intensity at the location of the LSPR of the elliptic ND grating clearly visible in the red part of the spectrum. Furthermore, the spectral map is affected by the SLRs originating from a coupling to the TM_0, TE_0, TM_1 modes traveling in *x*-direction (Fig. 7e, g) and the TM_0 mode along the y-direction (Fig. 7f, h). Again, as with the angle-resolved PL enhancement, a good match between the calculated and measured enhancement is obtained. We thus find clear signatures of the interaction between the gratings and the light modes in the WOLED stack and of the outcoupling of light.

4 Conclusion

In this work, we demonstrated a novel approach to enhance the broadband white light emission from a WOLED by a multipitch plasmonic particle grating consisting of regular arrays of elliptic and a circular Al NDs. We showed that embedding the superimposed grating within a layer of CuSCN effectively planarizes the surface which minimizes the risks of electrical shorts and shunt pathways and thereby leakage current and device failure. Embedding an Al ND array within a WOLED led to a current efficiency of the device enhanced by 23% even though the grating impaired the injection of holes. Through FDTD simulations, we achieved good agreement with the experimental measurements. The enhancement obtained in PL as well as in EL was found to correlate with the calculated field enhancement at the spectral positions of the SLRs. Angle-resolved PL and EL measurements yielded a good correlation between the calculated dispersion and the measured enhancement, thus confirming a coupling between the Al ND array and guided light modes in the WOLED stack. Our study validates the approach of using multipitched plasmonic particle gratings for broadband enhancement in WOLEDs. Further optimization of the grating geometry (lattice constants, particle sizes,

total surface coverage) as well as by choosing hole transport layers with a higher in-plane conductivity will allow for eliminating the observed injection barriers and thereby unlock the full potential of the provided concept.

Although not focused on in this study, it should be mentioned that our approach, besides efficiency enhancement, may also lay the foundation for a new strategy to enhance the white light quality of WOLEDs in the field of lighting. In a pioneering study, Thornton [37] has shown that by an appropriate and concerted choice of the wavelengths even the emission from three spectral lines can result in quite large values for the color rendering index. This approach, which to some extend also applies for only two, concerted, wavelengths [37, 38] subsequently, was used for the development of compact fluorescent lamps with high color rendering indexes. Future approaches for WOLED-based lighting devices may also benefit from these relationships and the use of two and more particle gratings. This could be done by an appropriate choice of the emitter materials in combination with the design of the shapes and sizes of the individual grating elements, so that light extraction becomes enhanced in concerted wavelength ranges that also support large color rendering index values. Although the latter, in principle, also could be achieved by an appropriate choice of the emission wavelengths of the emitter materials by its own, the combination with nanostructured gratings will allow to tune and enhance both, extraction efficacies and color rendering indices.

Declarations

References

1. M.J. Jurow et al., Understanding and predicting the orientation of heteroleptic phosphors in organic light-emitting materials. Nat. Mater. **15**, 85–91 (2016). https://doi.org/10.1038/nmat4428

2. H. Kaji et al., Purely organic electroluminescent material realizing 100% conversion from electricity to light. Nat. Commun. **6**, 8476 (2015). https://doi.org/10.1038/ncomms9476

3. C.Y. Chan, M. Tanaka, H. Nakanotani, C. Adachi, Efficient and stable sky-blue delayed fluorescence organic light-emitting diodes with CIEy below 0.4. Nat. Commun. **9**, 5036 (2018). https://doi.org/10.1038/s41467-018-07482-6

4. M.A. Baldo, M.E. Thompson, S.R. Forrest, High-efficiency fluorescent organic light-emitting devices using a phosphorescent sensitizer. Nature **403**, 750–753 (2000). https://doi.org/10.1038/35001541

5. C.F. Chang et al., Highly efficient blue-emitting iridium (III) carbene complexes and phosphorescent OLEDs. Angew. Chem. Int. Ed. **47**, 4542–4545 (2008)

6. K.-H. Kim et al., Phosphorescent dye-based supramolecules for high-efficiency organic light-emitting diodes. Nat. Commun. **5**, 4769 (2014). https://doi.org/10.1038/ncomms5769

7. G. Gomard, J.B. Preinfalk, A. Egel, U. Lemmer, Photon management in solution-processed organic light-emitting diodes: a review of light outcoupling micro- and nanostructures. J. Photonics Energy **6**, 030901 (2016)

8. M. Gather, S. Reineke, Recent advances in light outcoupling from white organic light-emitting diodes. J. Photonics Energy **5**, 057607 (2015)

9. J. Lin et al., Unprecedented homoleptic bis-tridentate Iridium(III) phosphors: facile, scaled-up production, and superior chemical stability. Adv. Func. Mater. **27**, 1702856 (2017). https://doi.org/10.1002/adfm.201702856

10. R. Mac Ciarnain et al., Plasmonic Purcell effect reveals obliquely ordered phosphorescent emitters in Organic LEDs. Sci. Rep. **7**, 1826 (2017). https://doi.org/10.1038/s41598-017-01701-8

11. J. Hauss et al., Metallic Bragg-gratings for light management in organic light-emitting devices. Appl. Phys. Lett. **99**, 103303 (2011). https://doi.org/10.1063/1.3631728

12. K. Ishihara et al., Organic light-emitting diodes with photonic crystals on glass substrate fabricated by nanoimprint lithography. Appl. Phys. Lett. **90**, 111114 (2007). https://doi.org/10.1063/1.2713237

13. P.Y. Ang, P.-A. Will, S. Lenk, A. Fischer, S. Reineke, Inside or outside: evaluation of the efficiency enhancement of OLEDs with applied external scattering layers. Sci. Rep. **9**, 18601 (2019). https://doi.org/10.1038/s41598-019-54640-x

14. Y. Motoyama et al., High-efficiency OLED microdisplay with microlens array. J. Soc. Inform. Display **27**, 354–360 (2019). https://doi.org/10.1002/jsid.784

15. N. Nakamura, N. Fukumoto, N. Wada, M. Ohgawara, Light extraction analysis of organic light emitting diodes fabricated on high refractive index glass scattering layer. J. Appl. Phys. **117**, 055502 (2015). https://doi.org/10.1063/1.4907396

16. S. Lloyd, T. Tanigawa, H. Sakai, H. Murata, Patterning of OLED glass substrate for improving light outcoupling efficiency. IEICE Trans. Electron. **E102.C**, 180–183 (2019). https://doi.org/10.1587/transele.2018OMS0010

17. S. Zou, N. Janel, G.C. Schatz, Silver nanoparticle array structures that produce remarkably narrow plasmon lineshapes. J. Chem. Phys. **120**, 10871–10875 (2004). https://doi.org/10.1063/1.1760740

18. V. Tretnak, U. Hohenester, J.R. Krenn, A. Hohenau, The role of particle size in the dispersion engineering of plasmonic arrays. J. Phys. Chem. C **124**, 2104–2112 (2020). https://doi.org/10.1021/acs.jpcc.9b10235

19. B. Auguié, W.L. Barnes, Collective resonances in gold nanoparticle arrays. Phys. Rev. Lett. **101**, 143902 (2008). https://doi.org/10.1103/PhysRevLett.101.143902

20. G. Vecchi, V. Giannini, J. Gómez Rivas, Shaping the fluorescent emission by lattice resonances in plasmonic crystals of nanoantennas. Phys. Rev. Lett. **102**, 146807 (2009). https://doi.org/10.1103/PhysRevLett.102.146807

21. S. Gerber et al., Tailoring light emission properties of fluorophores by coupling to resonance-tuned metallic nanostructures. Phys. Rev. B **75**, 073404 (2007). https://doi.org/10.1103/PhysRevB.75.073404

22. G. Lozano et al., Plasmonics for solid-state lighting: enhanced excitation and directional emission of highly efficient light sources. Light Sci. Appl. **2**, e66 (2013). https://doi.org/10.1038/lsa.2013.22

23. P.A. Hobson, S. Wedge, J.A.E. Wasey, I. Sage, W.L. Barnes, Surface plasmon mediated emission from organic light-emitting diodes. Adv. Mater. **14**, 1393–1396 (2002). https://doi.org/10.1002/1521-4095(20021002)14:19%3c1393::AID-ADMA1393%3e3.0.CO;2-B

24. R.F. Garcia et al., Enhanced electroluminescence of an organic light-emitting diode by localized surface plasmon using Al periodic structure. J. Opt. Soc. Am. B **33**, 246–252 (2016). https://doi.org/10.1364/JOSAB.33.000246

25. Y. Zakharko et al., Surface lattice resonances for enhanced and directional electroluminescence at high current densities. ACS Photonics **3**, 2225–2230 (2016). https://doi.org/10.1021/acsphotonics.6b00491

26. M.W. Knight et al., Aluminum for plasmonics. ACS Nano **8**, 834–840 (2014). https://doi.org/10.1021/nn405495q

27. S.J. Tan et al., Plasmonic color palettes for photorealistic printing with aluminum nanostructures. Nano Lett. **14**, 4023–4029 (2014). https://doi.org/10.1021/nl501460x

28. M. Auer-Berger, V. Tretnak, F.-P. Wenzl, J. Krenn, E.J. List-Kratochvil, Adjusting the emission color of organic light-emitting diodes through aluminum nanodisc arrays. Opt. Eng. **56**, 097102 (2017)

29. M. Auer-Berger, V. Tretnak, F.-P. Wenzl, J.R. Krenn, E.J.W. List-Kratochvil, Aluminum-nanodisc-induced collective lattice resonances: Controlling the light extraction in organic light emitting diodes. Appl. Phys. Lett. **111**, 173301 (2017). https://doi.org/10.1063/1.4998802

30. P. Pattanasattayavong, A.D. Mottram, F. Yan, T.D. Anthopoulos, Study of the hole transport processes in solution-processed layers of the wide bandgap semiconductor Copper(I) Thiocyanate (CuSCN). Adv. Func. Mater. **25**, 6802–6813 (2015). https://doi.org/10.1002/adfm.201502953

31. V.G. Kravets, A.V. Kabashin, W.L. Barnes, A.N. Grigorenko, Plasmonic surface lattice resonances: a review of properties and applications. Chem. Rev. **118**, 5912–5951 (2018). https://doi.org/10.1021/acs.chemrev.8b00243

32. T.V. Teperik, A. Degiron, Design strategies to tailor the narrow plasmon-photonic resonances in arrays of metallic nanoparticles. Phys. Rev. B **86**, 245425 (2012). https://doi.org/10.1103/PhysRevB.86.245425

33. Q. Fu, J. Chen, C. Shi, D. Ma, Solution-processed small molecules as mixed host for highly efficient blue and white phosphorescent organic light-emitting diodes. ACS Appl. Mater. Interfaces **4**, 6579–6586 (2012). https://doi.org/10.1021/am301703a

34. D. Gérard, S.K. Gray, Aluminium plasmonics. J. Phys. D Appl. Phys. (2015). https://doi.org/10.1088/0022-3727/48/18/184001

35. N. Koch, Electronic structure of interfaces with conjugated organic materials. Phys. Status Solidi (RRL) **6**, 277–293 (2012). https://doi.org/10.1002/pssr.201206208

36. N. Wijeyasinghe et al., p-Doping of Copper(I) thiocyanate (CuSCN) hole-transport layers for high-performance transistors and organic solar cells. Adv. Func. Mater. **28**, 1802055 (2018). https://doi.org/10.1002/adfm.201802055

37. W.A. Thornton, Luminosity and color-rendering capability of white light. J. Opt. Soc. Am. **61**, 1155–1163 (1971). https://doi.org/10.1364/JOSA.61.001155

38. M. Koedam, J.J. Opstelten, Measurement and computer-aided optimization of spectral power distributions. Light. Res. Technol. **3**, 205–210 (1971). https://doi.org/10.1177/096032717100300303